

An RF-Powered FDD Radio for Neural Microimplants

Yashar Rajavi, *Member, IEEE*, Mazhareddin Taghivand, Kamal Aggarwal, Andrew Ma,
and Ada S. Y. Poon, *Senior Member, IEEE*

Abstract—We present a radio system that could be used in millimeter-scale wireless neural implants. The system is RF-powered and demonstrates Mbps data rates required for neuromodulation and recording applications. The radio transmits at 58 Mb/s and receives at 2.5 Mb/s maximum data rates. The transceiver uses a duplexer to achieve full-duplex communication via frequency-division duplexing at 1.74 and 1.86 GHz for TX and RX, respectively. The average power consumption of the transmitter is 93 μ W at 58 Mb/s, while that of the receiver is 7.2 μ W at 2.5 Mb/s. The transceiver was fabricated using 40-nm LP CMOS process and occupies 0.8 mm² of die area. Including the off-chip duplexer, the system occupies 2 \times 1.6 \times 0.6 mm³.

Index Terms—Biomedical telemetry, energy harvesting, micro-electronic implants, neural prosthesis, radio transceivers.

I. INTRODUCTION

NEURAL implants are used to monitor and treat variety of medical conditions from heart arrhythmia to hearing loss [1], [2]. They are increasingly used in new applications such as brain-machine interface [3] and retinal prostheses [4]. All electronic body implants face two main challenges, among other ones, of power consumption and size. Long-term operation of the implants places a stringent requirement on power consumption. Although it is possible for batteries to supply uninterrupted power to certain kinds of implants for a finite duration, the use of batteries entails significant limitations for other kinds of applications. For example, a cardiac pacemaker is powered by a 0.5–2 Ah battery and lasts for 5–10 years [5]. A cochlear implant [6], however, drains the same battery in a few months. In addition, batteries are large and therefore significantly increase the overall system size. As shown in Fig. 1, even though the volume of implantable pacemakers has reduced considerably over the past decades [1], their size remains large, on the order of a few cm³. Reducing the size of these devices is highly desirable such that they could be implanted using less invasive surgical procedures. The aforementioned challenges have prompted the use of power harvesting to realize battery-less operation of the implants or reduce the battery volume. There exist several power harvesting techniques such as radio

frequency (RF), ultrasonic, optical, and so on [7]. RF-powering has been widely investigated for implants partly due to its reliability and easy integration with electronics. In addition, it can potentially provide a much needed data communication link. Commercial implants typically receive RF energy via inductive coupling at the HF band, for example, the 13 MHz ISM band. Nevertheless, to achieve high coupling efficiencies at these frequencies, the receiving coils are large. This in turn increases the overall size of the implant. Furthermore, high-data-rate (more than 1 Mb/s) communication is difficult because the available bandwidth at these frequencies is low. Therefore, to increase the data rate, higher order and complex modulation schemes should be employed. This increases the power consumption on both sides of the link. Unlike the common practice of RF-powering at the HF band through inductive coupling, wireless powering at low gigahertz frequencies has proven to deliver more power and penetrate deeper in tissue for small receiving coils [8]–[10]. For this to happen, the external antenna is designed to focus the EM waves at a certain depth similar to an optical lens [11]. Powering implants at gigahertz frequencies allow the receiver coils to shrink to millimeter-scale, hence reducing the overall implant size considerably. More available bandwidth at gigahertz frequencies enables higher data rates to achieve reasonable bit-error-rates (BERs) with simple modulation schemes, resulting in a more energy efficient overall communication link.

In this paper, we demonstrate a radio system that addresses the above design challenges [12]. The implemented system is fully RF-powered to eliminate the need for bulky batteries. In an implant application, similar to the RFID systems, an external reader with its antenna immediately on the skin would radiate enough RF energy in the direction of the implant to power it ON and to communicate data with it. The power delivery and downlink communication (from external reader to internal implant) use a 1.86-GHz carrier frequency to leverage optimal power delivery at low GHz frequencies. The downlink receiver (RX) data are amplitude-shift-keying (ASK)-encoded on the incident power carrier. On the uplink (communication from implant to the external reader), active transmission (TX) has been employed rather than backscattering. In backscattering (the most commonly used method in passive transmitters, such as RFIDs), the implant transmits data to the reader by reflecting the incident wave from the reader through the antenna load modulation. In this method, however, the receiver sensitivity of the reader is significantly degraded because the colocated high power transmitter falls in-band, hence, reducing the effective communication range [13], [14]. For

Manuscript received August 15, 2016; revised October 10, 2016 and December 12, 2016; accepted December 14, 2016. Date of publication February 2, 2017; date of current version April 20, 2017. This paper was approved by Guest Editor Danilo Manstretta.

The authors are with Stanford University, Stanford, CA 94305 USA, and also with Qualcomm Inc., San Jose, CA 95110 USA (e-mail: yrajavi@stanford.edu).

Color versions of one or more of the figures in this paper are available online at <http://ieeexplore.ieee.org>.

Digital Object Identifier 10.1109/JSSC.2016.2645601

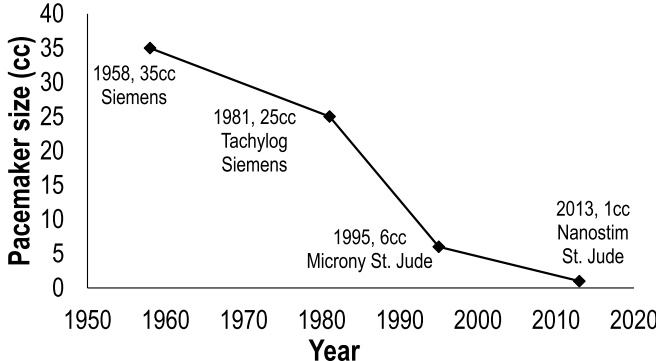


Fig. 1. Implantable pacemaker size reduction over past decades.

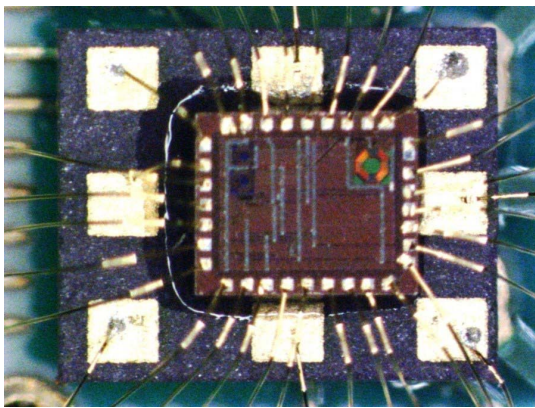


Fig. 2. Photograph of transceiver die stacked on top of duplexer.

example, assuming the reader has separate transmit and receive antennas with 10 dB of isolation between them and the transmitter outputs 30 dBm of power, the jammer power at the input of the reader's receiver will be 20 dBm. With such a high power jammer at its input, it is a huge challenge to receive the backscattered signal with a good sensitivity because of impairments such as large dc offset, intermodulation products, and front-end desensitization. On the other hand, in the active approach when using frequency division duplexing (FDD), because of the duplexer's band-to-band isolation, the reader's transmit power can be made high without having a concern on the linearity requirements of the reader's receiver. Also, active radios have been shown to support longer ranges [15], [16].

Since the prototyped implant is solely RF-powered, the RF signal must always stay active. In a microimplant platform using this radio system, the harvested RF energy powers not only the radio but also the peripheral sensors, stimulators, and actuators. If the RF signal disappears, the implant will stop working after the reservoir capacitor has been drained. It is therefore imperative for uplink and downlink communications to be carried out simultaneously or in quick succession. FDD which operates downlink and uplink at two different center frequencies satisfies this requirement. A compact $2 \times 1.6 \times 0.45$ mm³ duplexer separates the two frequencies with more than 50 dB of isolation [17]. This duplexer has an insertion loss of 2 dB on the TX path and 3 dB on the RX path. Fig. 2 shows

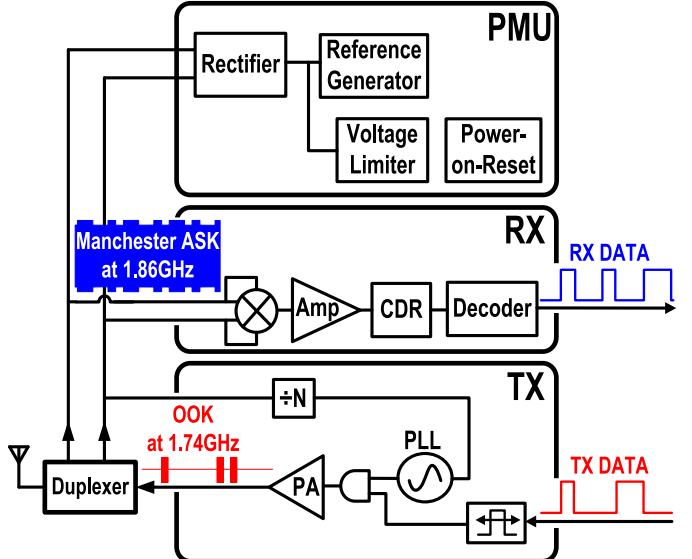


Fig. 3. Radio system block diagram.

the transceiver die stacked on top of the duplexer with a total size of $2 \times 1.6 \times 0.6$ mm³ system.

This paper is organized as follows. Section II introduces the prototyped radio system and describes its operation. Section III describes the circuit design of the transceiver. Section IV presents the experimental results and Section V concludes this paper.

II. SYSTEM OVERVIEW

Fig. 3 shows the block diagram of the prototyped radio system. The radio receives power from and exchanges data with an external reader. The overall system consists of a transceiver IC, a duplexer, and an antenna with the transceiver being the focus of this paper. The wireless transceiver consists of three functional units. The power management unit (PMU) is responsible for generating supply voltages, bias currents, and power-on reset (POR) signals needed by the rest of the chip. The receiver (RX), used for the downlink, amplifies and demodulates the ASK modulated data on the power carrier. The transmitter (TX) uses ON-OFF-keying (OOK) modulation for the uplink. The FDD full-duplex operation requires the RX and TX to operate at separate carrier frequencies. Therefore, the RX was chosen to operate at 1.86 GHz and the TX at 1.74 GHz. An OFF-chip duplexer combines the uplink and downlink streams together, and interfaces with the antenna. Gigahertz frequencies were selected to optimize power delivery inside biological tissue. The choice of frequencies was also influenced by the commercial availability of a compact duplexer.

III. CIRCUIT ARCHITECTURE

This section describes the circuit architecture of the transceiver IC functional units in more detail. First, the PMU as the unit responsible to supply power to the IC is described, followed by description, architecture, and operation of the RX. Finally, the topology and function of the TX is explained.

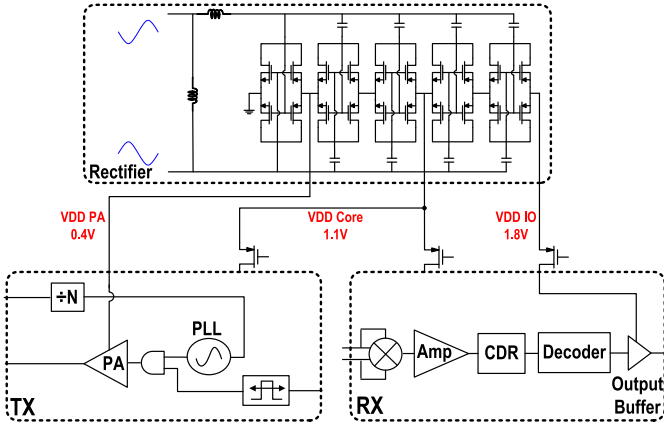


Fig. 4. Schematic of rectifier and transceiver power domains.

A. Power Management Unit

The PMU includes a rectifier, bandgap reference, supply voltage level detector, and POR circuitry. The rectifier converts the RF to dc. The full-wave CMOS rectifier is a five-stage charge-pump providing five voltage levels. Three of the five output voltages are tapped to supply different blocks in the transceiver. The output of the first stage, which is around 0.4 V, supplies the power amplifier (PA) in TX. Most other blocks are powered from the output of the third stage, which is around 1.1 V. The 1.8 V output of the fifth stage is used to supply power to peripheral sensors, stimulators, and actuators in a microimplant platform. In order to generate these voltage levels, the rectifier requires a voltage swing that is at least 0.5 Vpp at its inputs. Fig. 4 shows the rectifier and the corresponding power domains available on the transceiver IC. The RX uses 1.1 and 1.8 V supplies, while the TX uses the 0.4 and 1.1 V supplies. OFF-chip 100 nF capacitors are placed on the three supplies as charge reservoirs. If the RF power is momentarily cut off, these capacitors are able to keep the supply voltages within 10% of their nominal values for about 400 μ s at full operation. PMOS head-switches are used to turn individual functional units ON or OFF. An ON-chip impedance matching network at the input of the rectifier maximizes power transfer from the duplexer to the rectifier. Rectifier efficiency is directly related to the threshold voltages of the CMOS transistors in the charge-pump stages. To improve rectifier efficiency, deep N-well NMOS transistors have been used. By connecting the bulk to the source, the threshold voltage reduces thereby improving the RF-to-dc conversion efficiency. The simulated efficiency of the rectifier core, excluding the duplexer and the ON-chip matching network losses, is 65% at 3 dBm RF input power and 600 μ W load. Including the matching network loss, the efficiency is reduced to under 50%. Further, including the duplexer loss, the RF-to-dc conversion efficiency is below 25%.

Fig. 5 shows the schematic of the low-power bandgap reference. The output voltage of the block is set to 0.5 V. This block also provides bias currents for other circuits in the transceiver. Since the bandgap is the first block to turn ON after supply is up, it is essential to guarantee that it has settled

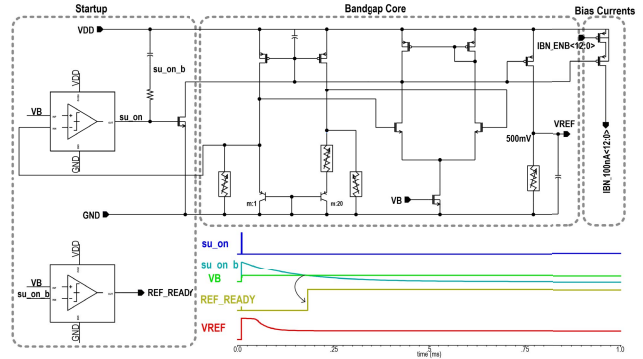


Fig. 5. Low-power bandgap reference (top) and simulated startup sequence (bottom).

before turning other blocks ON. Startup sequence is shown at the bottom of Fig. 5. VB is an arbitrary voltage generated ON-chip by a resistive ladder from the supply. REF_READY signal goes high slightly after $VREF$ has settled to 0.5 V. Bandgap power consumption is 500 nA, and the startup time is roughly 250 μ s.

Rectifier output voltage levels depend on the incident RF power. Therefore, if not enough power is received, the rectifier output voltages will be too low for the circuits to work. As a result, a supply voltage level detector was used to determine whether the supply voltages are within functional range. The circuit accommodates hysteresis by having two programmable voltage levels. Once the supply voltage crosses the first level, a SUP_READY signal is asserted. This signal is not set to low until the supply goes below the second programmable level. SUP_READY is used to turn ON/OFF the supply to RX and TX units.

If there is too much RF power at the rectifier input, the supply voltage levels may go too high and damage the internal circuits. A diode-based voltage limiter was connected to the 1.1 and 1.8 V supplies to limit the voltage in case these voltages go too high.

B. Receiver (RX)

Fig. 6 shows the block diagram of the RX unit. The RX receives ASK modulated data with Manchester-encoding on a 1.86 GHz carrier. The first block in the chain is a passive self-mixer that connects to the differential lines at the input of the rectifier. The rectifier requires a voltage swing that is at least 0.5 Vpp at its inputs to be able to generate the intended supply levels. This swing is already large enough for the self-mixer to perform the down-conversion without any need for an amplification stage. The self-mixer extracts the signal envelope. The signal at the input of the self-mixer is amplitude modulated (AM) and is represented by

$$v_{RF}(t) = A[1 + mx(t)] \cos(2\pi f_{RF} t) \quad (1)$$

where A is the amplitude of the RF carrier, m the AM modulation index, and $x(t)$ the envelope of the signal alternating between 0 and 1. Modeling the switching action of the self-mixer transistors to a periodic square pulse and only

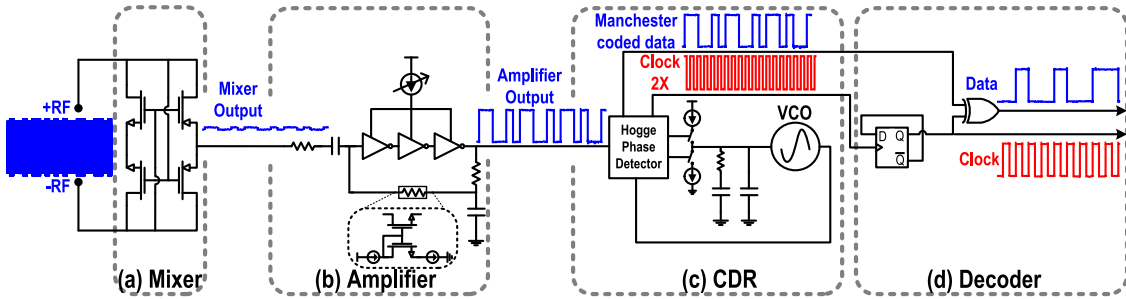


Fig. 6. Receiver chain block diagram. (a) Passive self-mixer. (b) Bandpass amplifier. (c) CDR. (d) Manchester decoder.

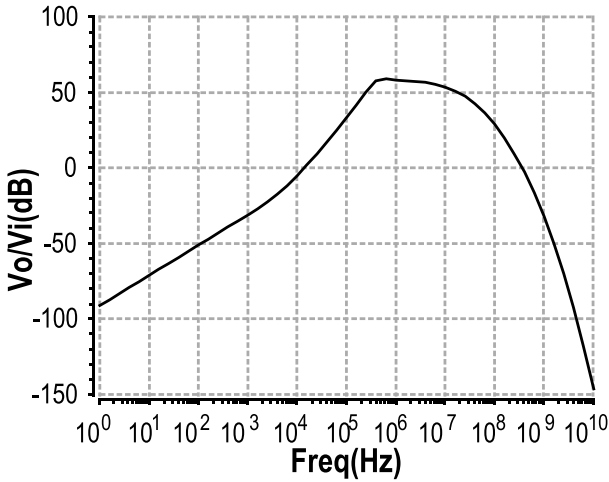


Fig. 7. RX bandpass amplifier simulated small-signal transfer function.

considering the fundamental harmonic, the signal at the output of the self-mixer can be written as

$$\begin{aligned}
 v_{RF}(t) &\times \frac{2}{\pi} \cos(2\pi f_{RF} t) \\
 &= \frac{2A}{\pi} [1 + mx(t)] \cos^2(2\pi f_{RF} t) \\
 &= \frac{A}{\pi} [1 + mx(t)] (1 + \cos(4\pi f_{RF} t)) \\
 &\xrightarrow{\text{low-pass filtering}} \frac{A}{\pi} [1 + mx(t)]. \quad (2)
 \end{aligned}$$

Therefore, the RF to baseband gain of the mixer is $1/\pi$. From (2), it becomes clear that $x(t)$ should not contain any valuable information at dc, because it would be masked by the large A/π dc component after self-mixing. In this design, we have used Manchester-encoding because its spectrum has no important component at dc [18]. Hence, the design is resilient to the large dc component generated from self-mixing. Manchester encoding is also good for the subsequent clock and data recovery (CDR) operation.

The mixer is followed by a low-power bandpass amplifier to filter noise and amplify the envelope signal to a CMOS rail-to-rail. It has a simulated small-signal peak gain of 56 dB and consumes 300 nA with low and high 3-dB frequencies of 320 kHz and 5.7 MHz, respectively. Fig. 7 shows the simulated transfer function of this amplifier.

A rail-to-rail signal at the output of the amplifier is input to a CDR circuit. As shown in Fig. 6(c), the CDR consists

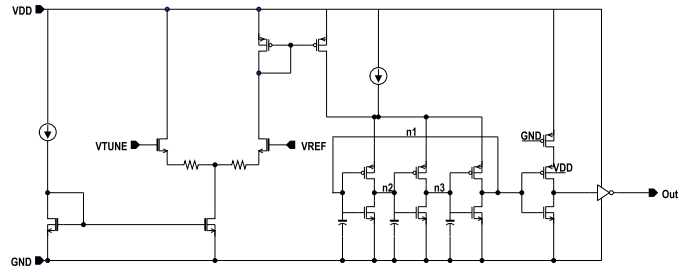


Fig. 8. VCO topology.

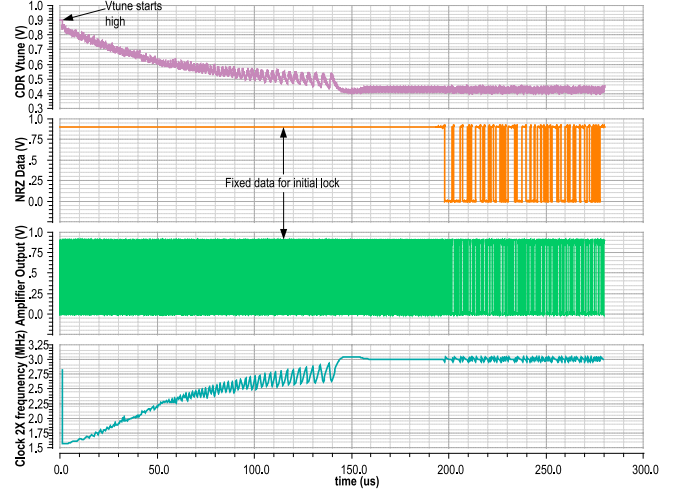


Fig. 9. Initial settling simulation of the CDR.

of a Hogge phase detector, a charge pump, a third-order loop filter, and a ring voltage-controlled oscillator. VCO topology is shown in Fig. 8. It uses three current-starved inverters connected in a loop to form an oscillator. VCO output frequency is at twice the RX data rate because of Manchester-encoding. VCO power consumption is $0.4 \mu\text{A}$ from 1.1 V . Fig. 9 shows initial transient simulation of the CDR. Initially, in order for the loop to lock, fixed data have to be applied to the CDR. This corresponds to a Manchester bitstream, which essentially is a clock running at the data-rate frequency. VCO control voltage also needs to be precharged to VDD . Once the loop has settled to the right frequency, the loop stays locked and data can be received. The CDR recovers Manchester-coded data and the corresponding $2\times$ clock signals from the input bit-

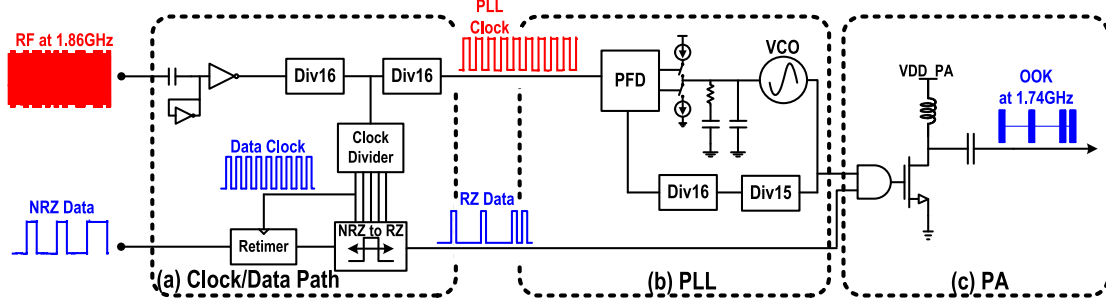


Fig. 10. Transmitter chain block diagram. (a) Clock and data path. (b) Integer- N PLL. (c) PA.

stream. In order to retrieve the initial non-return-to-zero (NRZ) bitstream, a simple Manchester decoder is used as shown in Fig. 6(d). Power consumption of the CDR is about $1 \mu\text{W}$.

RX supports data rates ranging from 1.5 to 2.5 Mb/s. Total measured power consumption of the RX is $7.2 \mu\text{W}$.

C. Transmitter (TX)

Fig. 10 shows the block diagram of the TX unit, which consists of a clock and data path block, an integer- N PLL, and a PA. TX modulation is return-to-zero OOK (RZ-OOK) on a 1.74 GHz carrier. Using OOK modulation results in a lower power consumption in a transmitter because the PA needs to be turned ON only for a short period of time for a few nanoseconds during a “1” pulse. The RF carrier is generated by an integer- N PLL. The PLL uses a ring oscillator topology as in Fig. 8. The reference clock to the PLL is at 7.2 MHz and is generated by dividing the 1.86-GHz RX carrier by 256 thereby eliminating the need for a large crystal resonator. Feedback ratio of the PLL divider is fixed at 240 setting the output frequency of the TX at 1.74 GHz. The PLL consumes $33 \mu\text{W}$. In OOK, the information is entirely encoded as changes in the amplitude of the carrier signal, therefore, the phase carries no information. As a result, the phase noise of the PLL can afford to be high and a very low power ring oscillator can be used. Furthermore, using an incoherent OOK receiver, there is no need to estimate carrier frequency or phase.

It would be possible to generate the TX carrier using only a free-running VCO as in [19]. However, without a PLL loop, the frequency could be outside the passband of the duplexer and the signal would have been completely attenuated. Additional tuning would be required to ensure the VCO frequency stays within range. In order to avoid this behavior, we use a PLL loop to guarantee that the TX carrier frequency is known. This comes at the cost of extra power consumption in the feedback and feedforward buffers, and frequency dividers. The frequency dividers are realized using the true single-phase clock logic with minimum size transistors to minimize power consumption.

The TX data, which is in NRZ format, is initially retimed by the output of the clock divider block. The programmable output frequency of the clock divider is $2^n \times 3.6 \text{ MHz}$ with $n = 1, 2, 3, 4$. The divider output can also be used as the sampling clock of an ADC on a peripheral sensor chip. An NRZ-to-RZ block follows the retimer. This block is

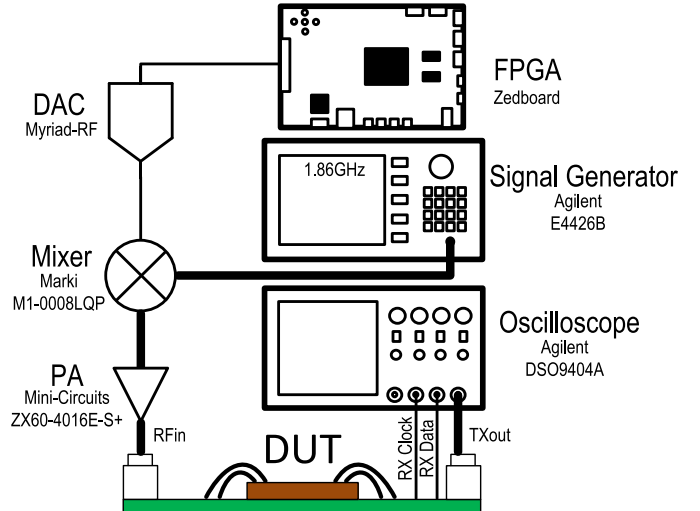


Fig. 11. Measurement setup.

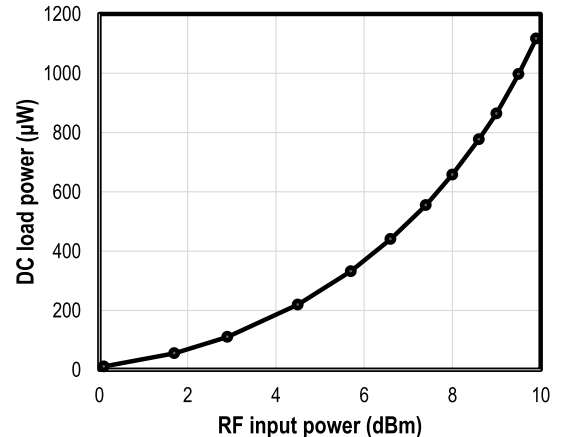


Fig. 12. Harvested dc power versus RF input power.

responsible for converting the retimed TX data from NRZ to RZ format. Its output is AND-gated with the output of the PLL to form the OOK modulated RF signal. Overall power consumption of clock/data-path block, as shown in Fig. 10(a), is $46 \mu\text{W}$ at maximum data rate of 58 Mb/s.

Since in OOK transmission data are modulated solely in amplitude, the PA does not need to be linear, hence switching PAs are suitable as they have higher efficiency. In this paper,

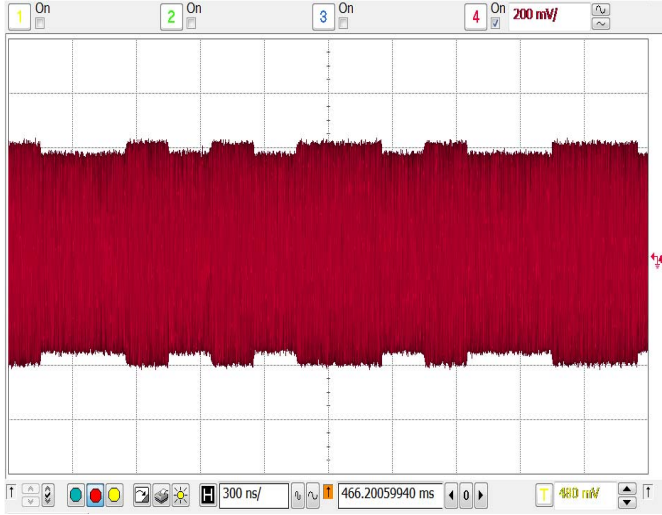


Fig. 13. RX input with Manchester-encoded data on a 1.86-GHz carrier.

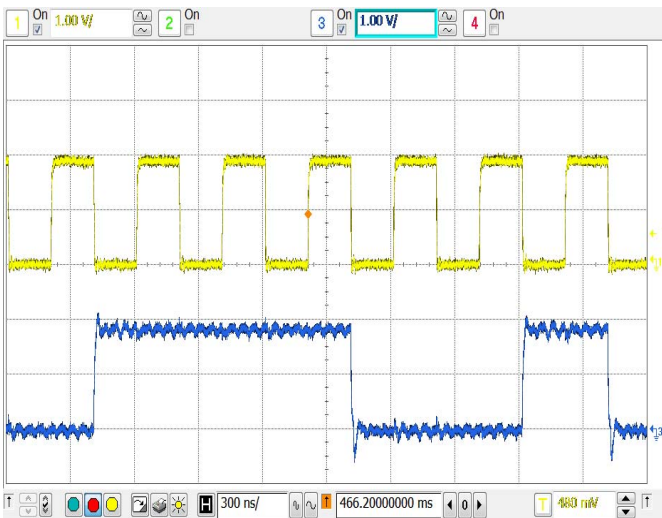


Fig. 14. Measured RX clock (top) and data (bottom) outputs for 2.5 Mb/s.

TABLE I
RX BER VERSUS MODULATION INDEX MEASUREMENTS
FOR 1.2 MB OF DATA AT 3 dBm RF INPUT POWER

Modulation Index (%)	Bit-error-rate (BER)
20	0
10	0
8	0
6	5.4×10^{-5}
4	0.16

we have used a class-E PA as shown in Fig. 10(c). When using midfield wireless powering at gigahertz frequencies, the path loss between the external reader and the implant is expected to be around 30 dB at a depth of 5 cm in tissue [11]. With an external reader sensitivity of -70 dBm (which is

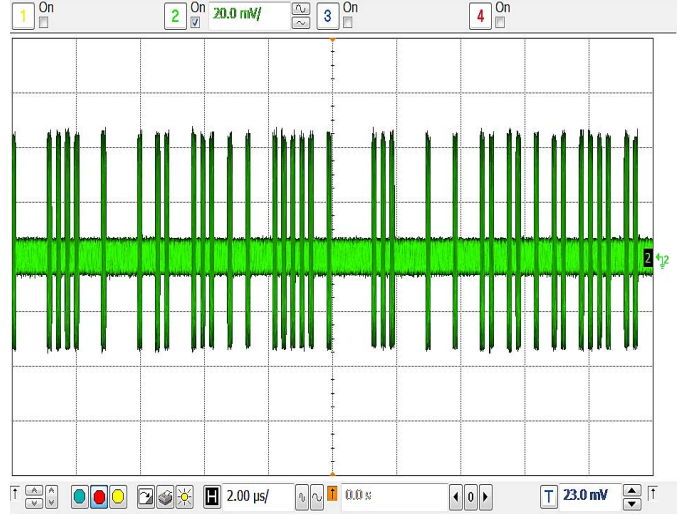


Fig. 15. Measured TX output for 3.6 Mb/s transmitting a pseudorandom sequence.

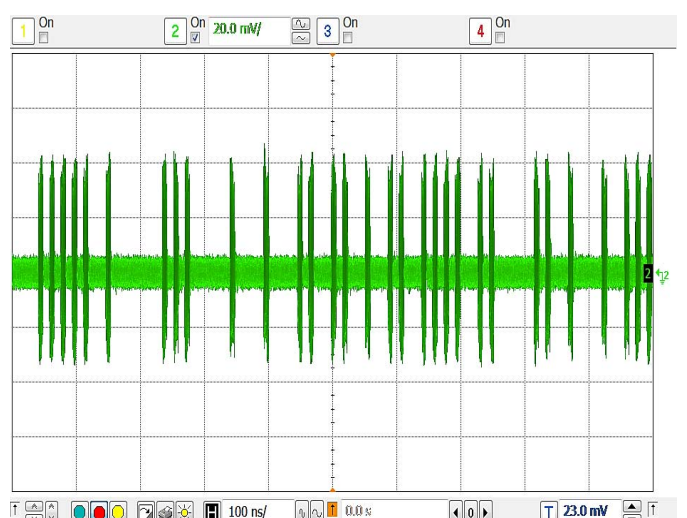


Fig. 16. Measured TX output for 58 Mb/s transmitting a pseudorandom sequence.

commercially available), the PA output power can be as low as -40 dBm. We added 20 dB of margin to achieve a power output of -18.5 dBm to account for antenna misalignments and other unforeseen loss mechanisms. Achieving good PA efficiency at such low output powers is not straightforward as most switching PAs are optimized for efficiency over 50% at output powers that are orders of magnitude above our desired level. One way to increase the PA efficiency is to lower the supply voltage of the PA. Since we are using a multistage charge-pump rectifier, we take the output of the first charge-pump stage as the PA supply voltage. The PA has a 20% measured drain efficiency from a 0.4 V supply. Measured output power of the PA to a $50\ \Omega$ load, not including the 2 dB duplexer loss, is -18.5 dBm when driven with a single-frequency signal.

The TX supports data rates from 3.6 to 58 Mb/s. The TX power consumption does not vary considerably with different

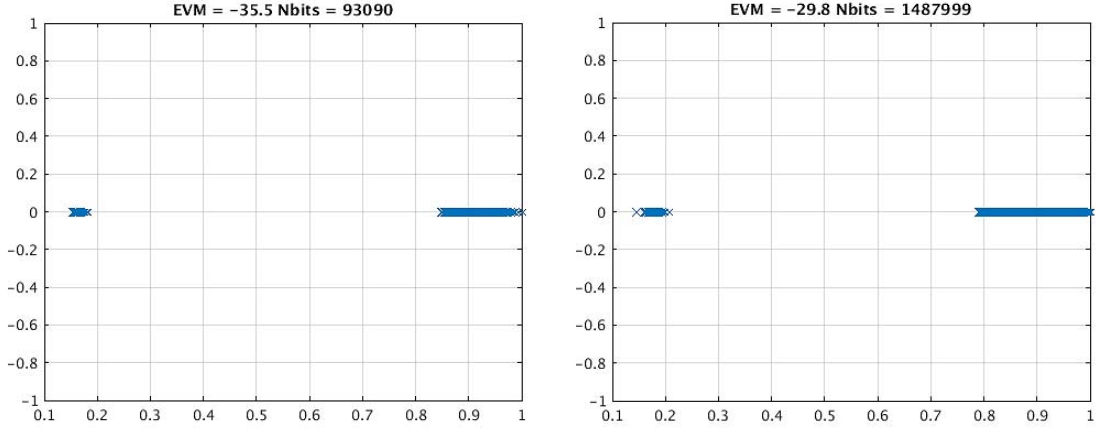


Fig. 17. TX output constellation for 3.6 Mb/s (left) and 58 Mb/s (right).

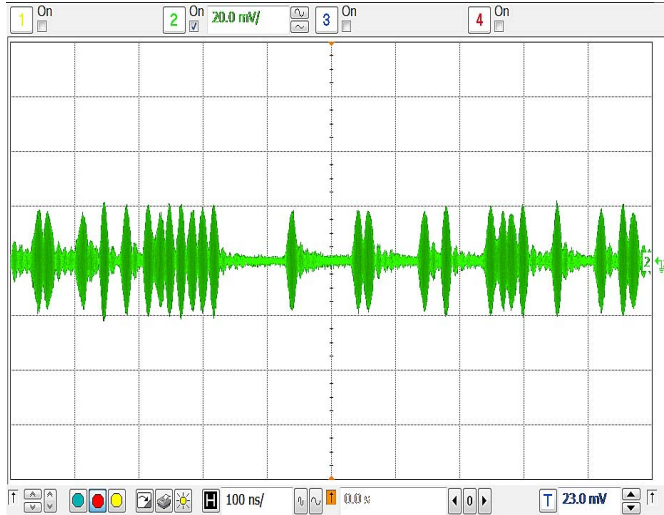


Fig. 18. Measured TX output for 58 Mb/s at the duplexer output.

data rates because it is dominated by the PLL and clock/data-path blocks. The TX consumes 79 μ W at 3.6 Mb/s and 93 μ W at 58 Mb/s.

IV. MEASUREMENT RESULTS

Fig. 11 shows the measurement setup. A field-programmable gate array (Zedboard) generates Manchester encoded ASK sequence which is up-converted to a 1.86 GHz carrier generated by the signal generator (Agilent E4426B) using a mixer component (Marki M1-0008LQP). The resulting signal is amplified using a PA (Mini-Circuits ZX60-4016E-S+) before being applied to the system. The chip decodes the received ASK signal and generates RX clock and data outputs which are captured using an oscilloscope (Agilent DSO9404A). A built-in 7-b pseudorandom sequence generator (PRBS7) is used to test the TX. The output of the TX is also captured by the oscilloscope. Postprocessing of the captured waveforms is done in MATLAB. The measurements are performed without using power supplies as the chip is RF-powered through the RF input port (RF_{in}).

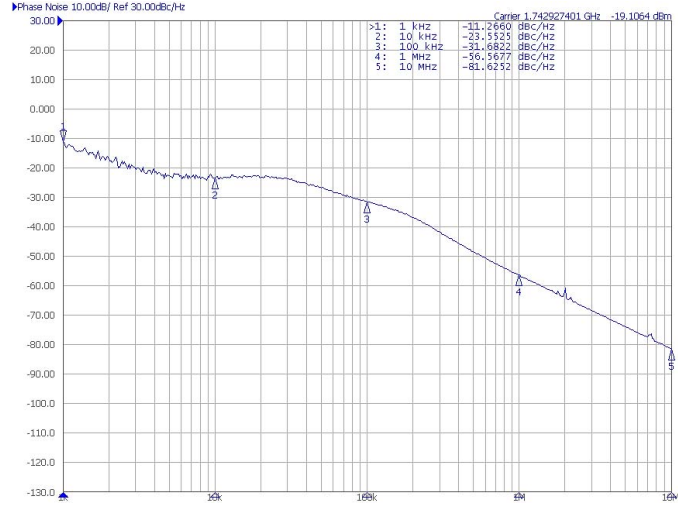


Fig. 19. Measured TX output phase noise spectrum.

Fig. 12 shows the harvested dc power versus RF input power. The duplexer has 3 dB of loss; therefore, the power that reaches the rectifier input will be 3 dB lower. For this measurement, all internal blocks are turned off and a variable dc current load is attached to the 1.1 V supply. Then, as the dc current load is increased, the input RF power is also increased until the rectifier output voltage reaches 1.1 V again.

Fig. 13 shows the RX input at 1.86-GHz carrier frequency with a 10% modulation index. The ripples on the carrier are the Manchester-encoded data stream. Fig. 14 shows an oscilloscope capture of the RX clock and data outputs at 2.5 Mb/s. Rising edge of the clock is used to sample the data. Table I lists RX BER versus modulation index for 1.2 Mb of data at 3 dBm RF input power. The RX sensitivity, not including the 3 dB duplexer loss, is estimated to be -25 dBm.

Fig. 15 shows the PA output waveform for 3.6 Mb/s. The TX is transmitting a PRBS7 pseudorandom sequence. The pulsewidth of the OOK signal is half of the bit time period, that is, 138 ns. The same waveform for 58 Mb/s can be seen in Fig. 16. In this case, the pulsewidth is 8.6 ns. Fig. 17 shows the constellation of the demodulated TX outputs for

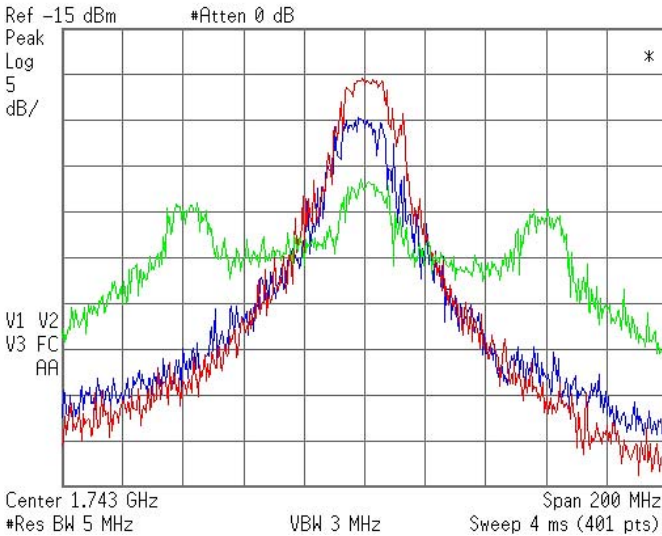


Fig. 20. Measured TX output spectrum for unmodulated (red), 3.6 Mb/s (blue), and 58 Mb/s (green).

TABLE II
PERFORMANCE SUMMARY AND COMPARISON WITH PRIOR ART

	This work	VLSI 2014 [20]	CICC 2014 [21]	ISSCC 2015 [22]	RFIC 2015 [23]
Carrier Frequency	RX 1850MHz TX 1750MHz	900MHz	915MHz	2440MHz	915MHz
Max. Data Rate	RX 2.5Mbps TX 58Mbps	200kbps	40.7kbps	7.8kbps 188kbps	20Mbps
Modulation Type	RX Manch. ASK TX RZ-OOK	PWM LSK	OOK	CDMA OOK	OOK
Active Power	RX 7.2μW TX 93μW	6μW	71.6μW	112nW 4.2μW	314μW
Energy Efficiency	RX 2.9pJ/bit TX 1.6pJ/bit	30pJ/bit	1.6nJ/bit 4.7nJ/bit	160pJ/bit 22pJ/bit	15.7pJ/bit
Sensitivity	RX -25dBm Pout TX -18.5dBm	-	-	-28.9dBm	-18.6dBm
EVM	RX TX -29.8dB	-	-	-	-

3.6 and 58 Mb/s. Error vector magnitude (EVM) is calculated to be at -35.5 and -29.8 dB for 3.6 and 58 Mb/s, respectively. The TX output waveform for 58 Mb/s at the duplexer output is shown in Fig. 18. The pulses become wider and EVM degrades to -22.1 dB because of the duplexer's limited bandwidth. Fig. 19 shows the phase noise spectrum of the TX output when transmitting the carrier signal without modulation. This phase noise plot by definition does not include the AM noise. Fig. 20 shows the spectrum of the TX output for unmodulated (red), 3.6 Mb/s (blue), and 58 Mb/s (green). The unmodulated TX output at 1.74 GHz has a wide bandwidth which is due to the large AM noise. The spectrum of the 3.6 Mb/s signal looks very similar to the unmodulated spectrum, because of the large wide-bandwidth AM noise that obscures the expected peaks at offsets of ± 3.6 MHz around the 1.74 GHz carrier. The lower peak power is expected, because, on average using RZ-OOK modulation, the PA is on 25% of the time which results in 6 dB lower average power compared with the unmodulated signal. The 58 Mb/s TX spectrum clearly shows the expected peaks at ± 58 MHz offsets from the carrier. The total integrated power for this

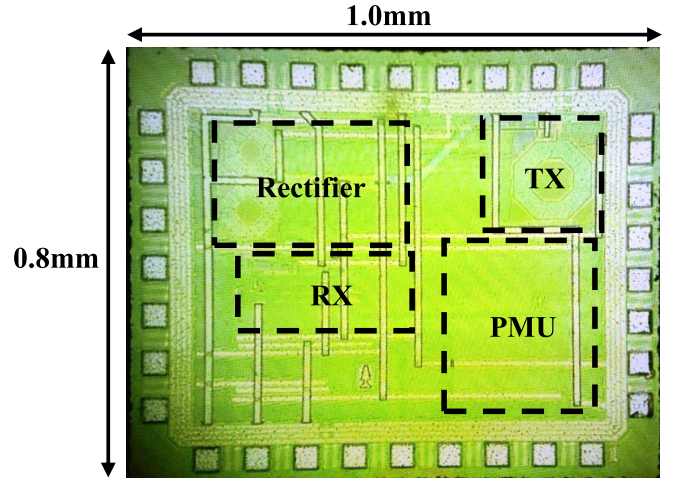


Fig. 21. Die micrograph of the proposed wireless transceiver.

signal should also be 6 dB lower than the power of the unmodulated carrier.

Table II summarizes the performance of the system and compares with state-of-the-art. Fig. 21 shows the die micrograph. The transceiver was fabricated in 40 nm CMOS and measures $1.0\text{ mm} \times 0.8\text{ mm}$ in area.

V. CONCLUSION

We have presented a wireless transceiver for neural implants. The transceiver enables low power and high data rate communication with the outside world while having a small form factor suitable for millimeter-scale implantable devices. The radio system is entirely RF-powered and supports full-duplex operation. The transceiver has recorded energy efficiency of 1.6 pJ/b for TX and 2.9 pJ/b for RX. This work enables wireless communication for miniaturized neural sensors and actuators with large number of channels and high data rate requirements.

ACKNOWLEDGMENT

The authors thank TSMC University Shuttle Program for IC fabrication, Lorentz Solution for EM software, and staff at Qualcomm Atheros in particular Mojtaba Sharifzadeh and Mo Ghahramani.

REFERENCES

- [1] St. Jude Medical, Inc. *Nanostim Leadless Pacemaker*, accessed on Aug. 2016. [Online]. Available: <http://media.sjm.com/newsroom/media-kits/arrhythmia-management/international/>
- [2] Med-El Corporation, *Cochlear Implants*. [Online]. Available: <http://www.medel.com/us/cochlear-implants/>
- [3] R. Muller *et al.*, "A minimally invasive 64-channel wireless μECOG implant," *IEEE J. Solid-State Circuits*, vol. 50, no. 1, pp. 344–359, Jan. 2015.
- [4] Second Sight Medical Products, Inc. *Argus Retinal Prosthesis System*. [Online]. Available: <http://www.secondsight.com/g-the-argus-ii-prosthesis-system-pf-en.html>
- [5] R. K. Shepard and K. A. Ellenbogen, "Leads and longevity: How long will your pacemaker last?" *Europace*, vol. 11, no. 2, pp. 142–143, 2009.
- [6] F. G. Zeng, S. Rebscher, W. Harrison, X. Sun, and H. Feng, "Cochlear implants: System design, integration, and evaluation," *IEEE Rev. Biomed. Eng.*, vol. 1, pp. 115–142, Nov. 2008.

- [7] B. A. Achraf, A. B. Kouki, and H. Cao, "Power approaches for implantable medical devices," *Sensors*, vol. 15, no. 11, pp. 28889–28914, 2015.
- [8] A. S. Y. Poon, S. O'Driscoll, and T. H. Meng, "Optimal frequency for wireless power transmission into dispersive tissue," *IEEE Trans. Antennas Propag.*, vol. 58, no. 5, pp. 1739–1750, May 2010.
- [9] S. Kim, J. S. Ho, and A. S. Y. Poon, "Midfield wireless powering of subwavelength autonomous devices," *Phys. Rev. Lett.*, vol. 110, no. 20, p. 203905, 2013.
- [10] J. S. Ho *et al.*, "Wireless power transfer to deep-tissue microimplants," *Proc. Nat. Acad. Sci. USA*, vol. 111, no. 22, pp. 7974–7979, Apr. 2014.
- [11] J. S. Ho, B. Qiu, Y. Tanabe, A. J. Yeh, S. Fan, and A. S. Y. Poon, "Planar immersion lens with metasurfaces," *Phys. Rev. B, Condens. Matter*, vol. 91, no. 12, p. 125145, 2015.
- [12] Y. Rajavi, M. Taghivand, K. Aggarwal, A. Ma, and A. S. Y. Poon, "An RF-powered 58Mbps-TX 2.5Mbps-RX full-duplex transceiver for neural microimplants," in *IEEE Radio Freq. Integr. Circuits Symp. (RFIC) Dig.*, Apr. 2016, pp. 234–237.
- [13] M. Mark *et al.*, "A 1mm^3 2Mbps 330fJ/b transponder for implanted neural sensors," in *Symp. VLSI Circuits Dig. Tech. Papers*, 2011, pp. 168–169.
- [14] G. Kim *et al.*, "A millimeter-scale wireless imaging system with continuous motion detection and energy harvesting," in *Symp. VLSI Circuits Dig. Tech. Papers*, Oct. 2014, pp. 1–2.
- [15] G. Chen *et al.*, "A cubic-millimeter energy-autonomous wireless intraocular pressure monitor," in *IEEE Int. Solid-State Circuits Conf. Dig.*, May 2011, pp. 310–312.
- [16] J. L. Bohorquez, A. P. Chandrasekaran, and J. L. Dawson, "A 350\textmu W CMOS MSK transmitter and 400\textmu W OOK super-regenerative receiver for medical implant communications," *IEEE J. Solid-State Circuits*, vol. 44, no. 4, pp. 1248–1259, Apr. 2009.
- [17] *B8088 SAW Duplexer Data Sheet*, EPCOS, Munich, Germany.
- [18] R. M. Gagliardi, "Modulation, encoding, and decoding," in *Satellite Communications*, 2nd ed. New York, NY, USA: Van Nostrand Reinhold, 1991, pp. 40–44.
- [19] M. Taghivand, K. Aggarwal, Y. Rajavi, and A. S. Y. Poon, "An energy harvesting 2×2 60 GHz transceiver with scalable data rate of 38–2450 Mb/s for near-range communication," *IEEE J. Solid-State Circuits*, vol. 50, no. 8, pp. 1889–1902, Aug. 2015.
- [20] M. H. Nazari, M. Mujeeb-U-Rahman, and A. Scherer, "An implantable continuous glucose monitoring microsystem in 0.18\textmu m CMOS," in *Symp. VLSI Circuits Dig. Tech. Papers*, Sep. 2014, pp. 194–195.
- [21] M. H. Ghaed, S. Skrzyniarz, D. Blaauw, and D. Sylvester, "A 1.6nJ/bit , 19.9\textmu A peak current fully integrated 2.5mm^2 inductive transceiver for volume-constrained microsystems," in *Proc. IEEE Custom Integr. Circuits Conf.*, Sep. 2014, pp. 1–4.
- [22] A. Klinefelter *et al.*, "A 6.45\textmu W self-powered IoT SoC with integrated energy-harvesting power management and ULP asymmetric radios," in *IEEE Int. Solid-State Circuits Conf. (ISSCC) Dig. Tech. Papers*, May 2015, p. 384.
- [23] M. S. Jahan, J. Langford, and J. Holleman, "A low-power FSK/OOK transmitter for 915 MHz ISM band," in *IEEE Radio Freq. Integr. Circuits Symp. (RFIC) Dig.*, Sep. 2015, pp. 163–166.



Yashar Rajavi (S'13–M'16) received the B.S. degree in electrical engineering from the University of Tehran, Tehran, Iran, in 2005, and the M.S. and Ph.D. degrees in electrical engineering from Stanford University, Stanford, CA, USA, in 2007 and 2016, respectively.

In 2007, he joined Atheros Communications (now Qualcomm Atheros), San Jose, CA, USA, where he designs analog, RF, and mixed-signal circuits for wireless applications. His current research interests include electronics for biomedical applications, wireless transceivers, and low-power design.



Mazhareddin Taghivand was born in Iran. He received the B.S. degree in electrical engineering from the California Institute of Technology, Pasadena, CA, USA, in 2004, the M.S. degree in electrical engineering from Harvard University, Cambridge, MA, USA, in 2006, and the Ph.D. degree in electrical engineering from Stanford University, Stanford, CA, USA, in 2015.

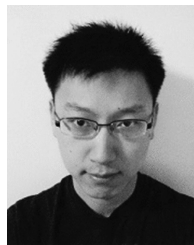
Since 2006, he has been with Qualcomm (now Qualcomm Atheros) Inc., San Jose, CA, USA, as an RF/Analog Engineer, where he is currently a Senior Staff/Manager, focusing on connectivity solutions. His current research interests include high-performance RF blocks, ultralow-power radios, and high-data rate communication at 60 GHz.



Kamal Aggarwal received the B.Tech. degree in electronics and communication engineering from the Dr. B. R. Ambedkar National Institute of Technology (NIT) Jalandhar, Jalandhar, India, in 2005, and the M.S. and Ph.D. degrees in electrical engineering from Stanford University, Stanford, CA, USA, in 2009 and 2016, respectively.

He has interned and was involved in different organizations focusing on various aspects of circuit design flow. At Infineon, Bangalore, India, he developed an optimization tool for initial circuit sizing of analog blocks. At Intel, Santa Clara, CA, USA, he was involved in the mask design for various blocks as well as developed tools to automate metal dummy insertion and schematic creation. During his internship with Rambus Inc., Sunnyvale, CA, USA, he developed a tool to automate layout migration among different process nodes along with the study of nonlinear noise modeling for voltage-controlled oscillator and phase-locked loop (PLL). He designed millimeter-wave power amplifiers and low-power PLLs for WiFi application during his internship at Qualcomm Inc., USA. He is currently a Teaching Assistant with Stanford University, Stanford, CA, USA, where he has taught analog and RF courses. His current research interests include millimeter-wave, RF, and analog and mixed signal circuit design.

Dr. Aggarwal was a recipient of the University Gold Medal at NIT, Jalandhar, in 2005, for securing highest GPA in the graduating class of 2005.



Andrew Ma received the B.S. degree in electrical engineering and computer sciences from the University of California, Berkeley, CA, USA, in 2009, and the M.S. degree in electrical engineering from Stanford University, Stanford, CA, USA, in 2011, where he is currently pursuing the Ph.D. degree with the Electrical Engineering Department.



Ada S. Y. Poon (S'98–M'04–SM'10) was born in Hong Kong. She received the B.Eng. and M.Phil. degrees in electrical and electronic engineering from the University of Hong Kong, Hong Kong, in 1996 and 1999, respectively, and the M.S. and Ph.D. degrees in electrical engineering and computer sciences from the University of California, Berkeley, CA, USA, in 1999 and 2004, respectively.

In 2004, she was a Senior Research Scientist at Intel Corporation, Santa Clara, CA, USA. In 2005, she was a Senior Technical Fellow at SiBeam, Inc., Fremont, CA, USA. From 2006 to 2007, she was an Assistant Professor at the Department of Electrical and Computer Engineering, University of Illinois at Urbana–Champaign, Champaign, IL, USA. Since 2008, she has been with the Department of Electrical Engineering, Stanford University, Stanford, CA, USA, where she is currently an Associate Professor. Her current research interests include applications of wireless communication and integrated circuit technologies to biomedicine and healthcare.